PNAS RESEARCH ARTICLE | ENGINEERING

Twisting for soft intelligent autonomous robot in unstructured environments

Yao Zhao[a], Yinding Chi[a], Yaoye Hong[a], Yanbin Li[a], Shu Yang[b], and Jie Yin[a,1]

Edited by John Rogers, Northwestern University, Evanston, IL; received January 11, 2022; accepted April 19, 2022

Soft robots that can harvest energy from environmental resources for autonomous locomotion is highly desired; however, few are capable of adaptive navigation without human interventions. Here, we report twisting soft robots with embodied physical intelligence for adaptive, intelligent autonomous locomotion in various unstructured environments, without on-board or external controls and human interventions. The soft robots are constructed of twisted thermal-responsive liquid crystal elastomer ribbons with a straight centerline. They can harvest thermal energy from environments to roll on outdoor hard surfaces and challenging granular substrates without slip, including ascending loose sandy slopes, crossing sand ripples, escaping from burying sand, and crossing rocks with additional camouflaging features. The twisting body provides anchoring functionality by burrowing into loose sand. When encountering obstacles, they can either self-turn or self-snap for obstacle negotiation and avoidance. Theoretical models and finite element simulation reveal that such physical intelligence is achieved by spontaneously snapping-through its soft body upon active and adaptive soft body-obstacle interactions. Utilizing this strategy, they can intelligently escape from confined spaces and maze-like obstacle courses without any human intervention. This work presents a de novo design of embodied physical intelligence by harnessing the twisting geometry and snap-through instability for adaptive soft robot-environment interactions.

autonomous soft robot | physical intelligence | unstructured environment | liquid crystal elastomer | snapping

Significance

Autonomy is crucial for soft robotics that are constructed of soft materials. It remains challenging to create autonomous soft robots that can intelligently interact with and adapt to changing environments without external controls. To do so, it often requires an analogical soft "brain" that integrates on-board sensing, control, computation, and decision-making. Here, we report an autonomous soft robot embodied with physical intelligence for decision-making via adaptive soft body-environment interactions and snap-through instability, without integrated sensing and external controls. This study harnesses physical intelligence as a new paradigm for designing autonomous soft robots that can interact intelligently with their environments, thus potentially reducing the burdens on the conventional integrated sensing, control, computations, and decision-making systems in designing intelligent soft robots.

Twisted and helical structures are one of the most common structural motifs in biology and ubiquitous in our lives, from DNA strands to climbing vines of plants and drill bits, to metallic colored beetle scales and spiral staircase. They offer a one-dimensional geometry that can pack a large group of functional units in a confined three-dimensional (3D) space. They have been integrated with soft materials for diverse applications in soft robotics, including grippers (1–5), artificial muscles (6–8), human-robot interfaces (9), microswimmers (10–13), and rolling robots (14–18). Among different soft actuating materials, anisotropic smart materials such as liquid crystal polymers (LCPs) (4, 5, 19–23) and magnetic elastomers (10–13, 24, 25) hold great potential in designing autonomous soft robots (26–28). They can harvest environmental sources, such as light, heat, and magnetic field for potentially untethered, adaptive locomotion and manipulation (4, 5, 10–18, 23–25, 29–31), without the need of cumbersome, tethered or on-board power and controls.

The helical and twisted structures often take two shapes: helical ribbons (i.e., spring-like coiled ribbons without twisting or helical tubular rods, both have a helix centerline) and twisted ribbons (i.e., drill bits-like twisted ones with a straight centerline) as shown in *SI Appendix*, Fig. S1. Both 3D ribbon shapes made of LCPs can be achieved by transforming from a flat twist-nematic-elastomer strip with a chiral dopant (5, 32) or flat nematic bilayer strip with an angular director orientation offset (4) in response to temperature change or light irradiation. Based on the transformed helical ribbons, recent studies have demonstrated their subsequent light-induced or temperature-induced directional self-rolling and slope-climbing motions on flat, hard surfaces in azobenzene-functionalized LCP ribbons and printed bilayer LCP ribbons (14, 17, 18). Similar stimuli-responsive self-rolling motion on flat surfaces is also achieved in an LCP rod (30), ring (33), and pentagonal prism (34). To date, most studies focus on shape transformation of these helical, tubular, and ring ribbons and their interactions with smooth contact boundaries (14–18, 30, 33). The study on how to utilize the twisted ribbons with distinct blade-like sharp contact boundaries for high-performance motion remains largely unexplored (35).

We note that most of the demonstrated self-rolling motions are on flat, hard surfaces (14–18, 30, 33, 34). It remains a grand challenge in soft robots to achieve autonomous locomotion in various unstructured environments (26–28), including the more challenging granular terrains (e.g., loose sand and rocks) (36) and environments with

Author affiliations: [a]Department of Mechanical and Aerospace Engineering, North Carolina State University, Raleigh, NC 27695; and [b]Department of Materials Science and Engineering, University of Pennsylvania, Philadelphia, PA 19104

Author contributions: Y.Z. and J.Y. designed research; Y.Z., Y.C., and Y.H. performed research; Y.Z., Y.C., Y.H., Y.L., S.Y., and J.Y. analyzed data; and Y.Z., S.Y., and J.Y. wrote the paper.

The authors declare no competing interest.

This article is a PNAS Direct Submission.

Copyright © 2022 the Author(s). Published by PNAS. This article is distributed under Creative Commons Attribution-NonCommercial-NoDerivatives License 4.0 (CC BY-NC-ND).

[1]To whom correspondence may be addressed. Email: jyin8@ncsu.edu.

This article contains supporting information online at http://www.pnas.org/lookup/suppl/doi:10.1073/pnas.2200265119/-/DCSupplemental.

Published May 23, 2022.

Downloaded from https://www.pnas.org by 98.122.129.244 on March 31, 2023 from IP address 98.122.129.244.

obstacles (e.g., mazes or obstacle courses), where the capabilities such as autonomously adapting to changing terrains and negotiating and avoiding obstacles as demonstrated here, are highly desired. It requires a sophisticated "brain" that integrates sensing, learning, control, computation, and decision-making (27). To date, most of the demonstrated untethered soft robots or machines made of either magneto-elastomers or LCPs interact with environments rather passively, since they predominantly rely on the external controls of the remote magnetic field or light sources to direct their actuation behavior and control their locomotion (10–17, 23–25, 29–31). In contrast, biological counterparts can actively and intelligently deform their bodies to avoid obstacles, move across hot, loose and slippery terrains [e.g., sidewinding desert snakes (37)], or escape from small confined spaces.

Here, we report harnessing twisted liquid crystal elastomer (LCE) ribbons with embodied physical intelligence (PI) (38) for constructing a simple potential intelligent autonomous soft robot. Different from neuron-based computational intelligence through the brain, PI leverages structural designs and smart materials to physically encode sensing, actuation, control, adaptation, and decision-making etc. into the body of an agent (38). The stimuli-responsive body materials can enable autonomous sensory, actuation, powering, and other PI functions (38). Similar to the first electronic autonomous robots named Elmer and Elsie (39) that responded to environmental stimuli such as light or mechanical touch to avoid obstacles, the twisted LCE ribbon here acts as a simple autonomous and intelligent soft robot. It utilizes adaptive soft body-environment interaction-based PI functions to create autonomous responses without any human intervention and external control. As seen in Fig. 1 *A* and *B* and later, the twisted LCE ribbon is capable of self-sensing environmental temperature change, untwisting itself for self-rolling, self-adapting to changing granular terrains, self-rotating and self-snapping its soft body for obstacle negotiation and avoidance, and self-solving and escaping of simple maze-like obstacle courses.

Results

Fabrication and Characterization of Twisted LCE Ribbons. The twisted LCE ribbons are simply fabricated by mechanically stretching and twisting of a rectangular flat LCE strip with length l and width w ($l/w \gg 1$) synthesized in two-stage polymerization (40, 41) (Fig. 1*C*) (see details in *Materials and Methods*). Stretching makes the mesogens aligned along with the stretching direction. When further twisted, a 3D mesogen alignment with twisted morphology is obtained (32) (Fig. 1*C*, Right). The nematic-isotropic transition temperature (T_{NI}) of the as-synthesized LCE is about 80 °C (*SI Appendix*, Fig. S2*A*).

Fig. 1*D* shows that as the environmental temperature increases from the room temperature (23 °C) to above T_{NI}, the freely hanging twisted LCE ribbons become untwisted and shrunk in length. The twist number n (Fig. 1*E*) decreases and the nominal strain ε (Fig. 1*F*) shrinks moderately at T_{NI} but dramatically above T_{NI}, 140 °C. Overall, they shrink slightly less (ε ~40% at 140 °C, Fig. 1*F*) compared to their flat counterparts (ε ~46% at 140 °C, *SI Appendix*, Fig. S2*B*) given their twisted geometries. While the length is shrunk, the ribbon is untwisted, leading to a dramatic increase of the pitch p when heated above T_{NI} (*SI Appendix*, Fig. S3). The observed untwisting and length shrinkage with the elevation of temperature are well reproduced by the corresponding finite element analysis (FEA) simulation (Fig. 1*G*) (see details in *Materials and Methods*). After cooling down to room temperature, the ribbons can fully recover to their initial twisted shapes attributed to the two-way shape memory effect of LCEs (42, 43).

Autonomous Rolling and its Mechanism. When the twisted LCE ribbon is placed on a hotplate above T_{NI}, it can roll autonomously and continuously driven by the dynamically changing discrete thermal contacts of the edges (Fig. 2 *A–D*, Movies S1 and S2). The self-rolling is accompanied by slight bending of the centerline (red dashed line in Fig. 2*A*) and global untwisting (Fig. 2 *E* and *F*). In contrast, the spring-like helical LCE ribbon, fabricated by simply wrapping around a cylindrical rod without twisting, becomes flattened and fails to self-roll (*SI Appendix*, Fig. S4), due to the lack of twisted nematic alignment (14, 17, 18). The curved centerline of the twisted ribbon remains bended toward the rolling direction during motion. The rolling direction is independent of its twisting chirality and always follows the same direction as the convex orientation of the curved centerline (*SI Appendix*, Fig. S5, Movie S1). The rolling behavior is similar to that of self-rolling LCE cylindrical rods on a hot plate (30) and self-rolling azobenzene-based helical LCP ribbons but with a concave shape toward lights (14). Thus, the rolling direction can be reverted on the fly by manually flipping its curved soft body back and forth using a tweezer (*SI Appendix*, Fig. S5, Movie S1). Like the homogeneously heated free-hanging twisted ribbons, the self-rolling twisted ribbon on the hot plate also shrinks in length and untwists itself with the twist number reduced from 6 to a stabilized 2 (Fig. 2*F*).

The average self-rolling speed of the twisted ribbons is mainly determined by the temperature of the hot surfaces, rather than the twist density defined as the number of turns per centimeter shown in Fig. 2*G*. When the surface temperature increases from 80 °C to 180 °C, the rolling speed of the ribbon (e.g., a twist density of 0.5 turn/cm in Fig. 2*G*) is more than doubled, from ~1.5 mm/s to ~3.8 mm/s. Although a higher twist density renders more thermal contact points, it does not necessarily increase the average rolling speed.

Fig. 2*B* shows the front-view images of slow-motion, time-lapsed rolling ribbon during one cycle of rolling (Movie S1). As it rolls, the center part of its soft body pops up (Fig. 2*B*, *ii*) and loses the thermal contact (highlighted in dashed circles in Fig. 2*B*, *i*). This is attributed to the out-of-plane buckling caused by the discrete localized thermal contacts induced shrinking of the LCE. Consequently, it falls forward driven by the off-center gravity with new engaging contact edges and the number of discrete edge contacts is recovered (Fig. 2*B*, *iii-iv*). The rolling motion captured by an infrared camera (Fig. 2*C* and Movie S2) shows that it induces a thermal gradient along the ribbon width that decreases from 110 °C at the small contact region (point a) to 90 °C at the outer boundary (point b) (Fig. 2*D*). In this way, the rolling twisted ribbon conserves a relatively lower temperature distribution throughout its main soft body in the range of about 90 °C to 100 °C to avoid overheating, except at the discrete small contact regions, much like the sidewinding snake.

Mechanically, the observed untwisting during self-rolling is attributed to different spin angular velocities at two free ends. As illustrated in Fig. 2*E*, upon thermal contact, both free ends undergo local untwisting but in opposite spin directions, where the top end untwists clockwise while the bottom end spins counterclockwise, the same as the global rolling direction of the ribbon. In the beginning, the bottom end spins faster than the top end, causing untwisting of the ribbon (Fig. 2*F*). After that,

Downloaded from https://www.pnas.org by 98.122.129.244 on March 31, 2023 from IP address 98.122.129.244.

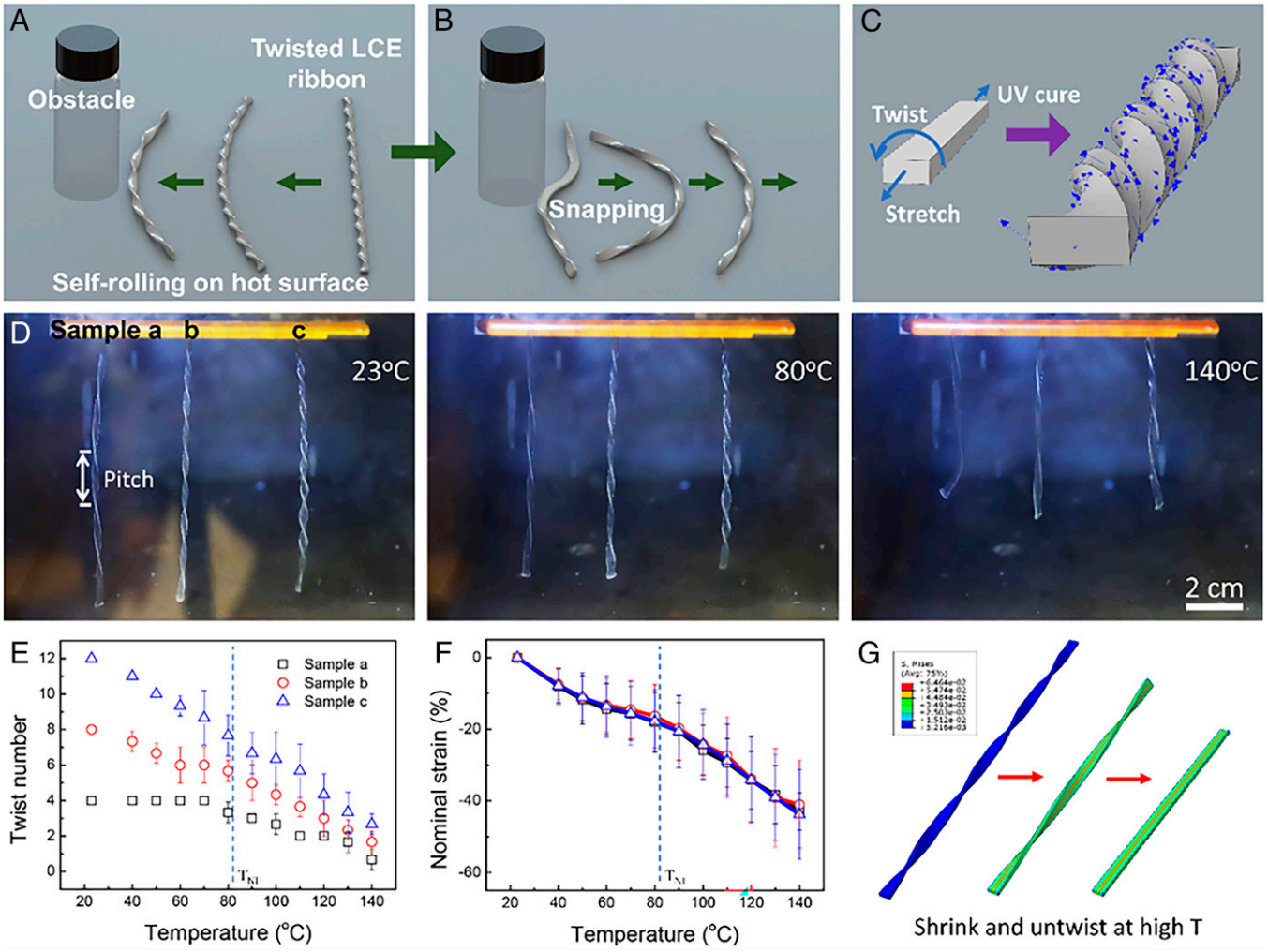

Fig. 1. Environment-responsive soft robots constructed from twisted LCE ribbons with a straight centerline. (*A* and *B*) Schematics of a self-rolling soft robot on hot surfaces accompanied by spontaneously and slightly bended soft body shape (*A*), and active reaction to obstacles via snapping its soft curved body to revert its rolling direction to autonomously avoid the obstacle (*B*). (*C*) Schematics of fabricating the twisted LCE ribbons by stretching and twisting a planar ribbon following two-stage reaction methods. The right arrows denote the orientations of the simulated maximum principal stresses in the twisted LCE ribbon. (*D*) Shape changes of three samples with different twist densities with the environmental temperature changing from room temperature (*Left*) to near the nematic-isotropic transition temperature T_{NI} = 80 °C (*Middle*) and above T_{NI} (*Right*). (*E* and *F*) Characterization of thermal responsiveness of three samples in terms of twist number (*E*) and nominal strain (*F*). (*G*) FEA simulation of the combined thermal shrinkage and untwisting process at higher temperatures.

the dynamic heating and cooling of the ribbon reach thermodynamic equilibrium, where both free ends spin at the same angular velocity. Therefore, no further untwisting occurs, and the ribbon keeps rolling with a constant twist number (Fig. 2*F*).

We find that there exists a wide surface temperature range (i.e., 55 °C to 220 °C, temperature profiles shown in *SI Appendix*, Fig. S6) to drive the continuous self-rolling of the twisted ribbons from even below T_{NI} to much above T_{NI}. Fig. 2*G* shows that at 55 °C, a temperature below T_{NI} ~80 °C, the ribbon can still continuously self-roll but with a rather slow speed of ~0.5 mm/s. Further lowing the temperature below 55 °C cannot provide sufficient force to drive the continuous motion. When temperature is increased far above T_{NI} (e.g., over 220 °C), the LCE ribbon becomes completely untwisted into a flat strip and can no longer roll.

As a proof-of-concept energy harvesting from natural environment, we directly placed the twisted LCE ribbon on an outdoor car roof on a sunny day with an ambient temperature of 27 °C (12:08 PM on June 1, 2021, Raleigh, NC, USA). Fig. 2*H* and Movie S3 show that it self-rolled continuously to climb the slightly curved car roof with an average speed of 0.4 mm/s. The roof surface temperature fluctuated between 78 °C and 85 °C due to the movement of the clouds.

Cargo Transport and Autonomous Rolling in Various Unstructured Terrains. We then exploit the cargo manipulation and debris cleaning functionality as a result of the locomotion of the soft robot (Movie S4). Fig. 3*A* shows that a lightweight aluminum tube (0.3 g) can be continuously pushed forward by the ribbon of a similar mass (0.36 g). When placing a glass vial (diameter of 2 cm) or a tweezer at the right end of the ribbon to block its forward rolling, the translation motion is switched to rotation, sweeping clockwise and collecting the randomly distributed aluminum particles (Fig. 3*B* and *SI Appendix*, Fig. S7). Once all the particles are piled together, the glass vial is removed, and the soft robot keeps pushing the debris forward to clean the area (Fig. 3*B* and Movie S4).

Next, we explore the potential of locomotion in various unstructured terrains, including granular substrates such as flat loose sand, sand dunes, uneven loose sand with randomly distributed bumps and pits, and tiny rocks, as well as mesh-like discrete surfaces such as grills (Fig. 3 *C*–*G*, Movie S5, see

Downloaded from https://www.pnas.org by 98.122.129.244 on March 31, 2023 from IP address 98.122.129.244.

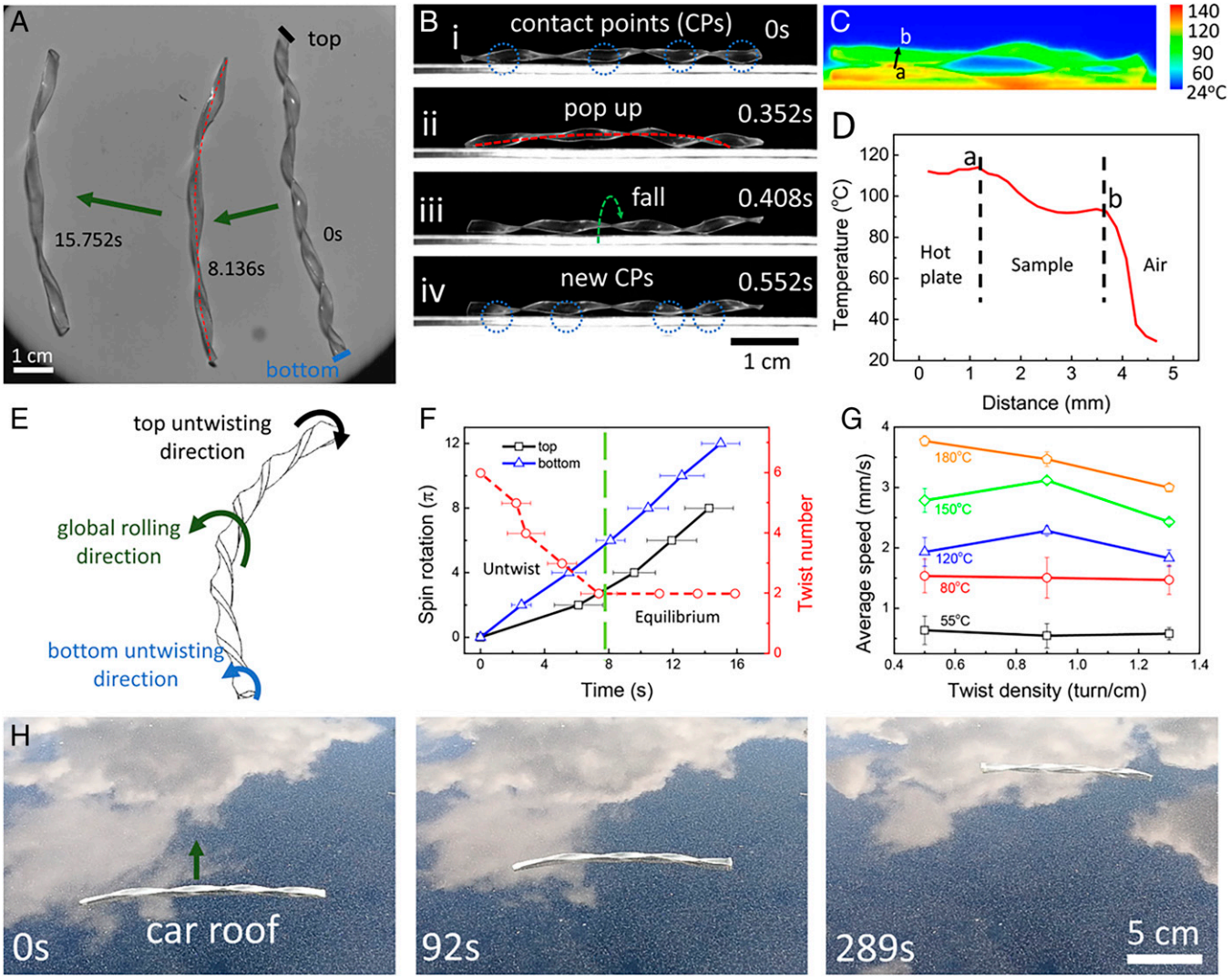

Fig. 2. Self-rolling twisted LCE ribbons on a hot plate and a car roof. (*A*) Top-view overlapped time-lapse images of self-rolling twisted ribbon on a hot plate at 150 °C. The original straight centerline bends spontaneously toward the rolling direction. The twist number reduces from 6 to a stabilized number of 2. (*B*) Front-view time-lapse images of self-rolling ribbon in one rolling cycle. Initially, it has four discrete thermal contact points (CPs) (*i*), and it buckles and pops up to lose the center CPs (*ii*), followed by falling toward the rolling direction (*iii*) with recovered new CPs (*iv*). (*C* and *D*) The infrared image of temperature field of the rolling ribbon on a hot plate. The temperature profile along path a-b is shown in (*D*). It shows a gradient temperature distribution along the width. (*E* and *F*) Schematics of opposite untwisting directions in the forward rolling ribbon at two ends (*E*) with its angular velocity (spins vs. time) and twist number changes shown in (*F*). The faster spinning at the bottom end results in the untwisting and reduced twist number in the first duration of about 8 s, followed by the same spinning speeds of two ends for a constant and stabilized twist number of 2. (*G*) Effects of surface temperature (from 55 °C, below T_{NI} to 180 °C, well above T_{NI}) and twist densities on the average rolling speed. A higher surface temperature leads to a faster speed, but a higher twist density does not warrant a faster speed despite more thermal contact points. (*H*) Demonstration of self-rolling on climbing a car roof in outdoor environment (air temperature of 27 °C and surface temperature ~80 °C). The average rolling speed is 0.4 mm/s. Cloud movement (white region) is reflected on the car roof.

Materials and Methods for more details on the setup of various terrains). Unlike the hard surfaces, locomotion on granular terrains is rather challenging (36), especially in sand dunes with fluid-like discrete solid particles and hostile environments such as desert with high temperature. Legged, jamming or sidewinding locomotion is often employed in soft robots on granular substrates (44, 45). For example, desert snakes employ sidewinding to slither sideways across loose and hot sands at a fast speed (37), thus, they effectively avoid sinking/slipping and reduce body contact with hot sand.

Here, we exploit the unique twisted boundary of the rolling LCE ribbons, as the analogous caterpillar treads that are often equipped in wheeled robots or vehicles (46, 47), to reduce slipping on granular substrates. Our ribbon can self-roll on hot, flat, dry loose sand with both coarse and fine sand grains without getting stuck (SI Appendix, Fig. S8), where the depth of loose sand is much larger than the diameter of the ribbon (3 mm). Notably, it is capable of ascending a loose sand dune with an inclined angle of 15° without slipping (Fig. 3*C*), where the imprints in the tracks can be clearly seen despite its light weight (a mass of 0.36 g). The imprints indicate that the twisted ribbon burrows into the loose sand for an enhanced traction through the dynamic, discrete thermal contacts of its drill bits-like blades with the sand, which can effectively reduce the slipping. This is in sharp contrast to the smooth contact boundaries of the self-rolling rods, helical ribbons, and rings on flat, hard surfaces (14–18, 30, 33) via shrinkage along the tubular ring diameter or the axial length. As seen in Fig. 3*D*, our ribbon can also cross the peaks and valleys of periodic wavy sand terrains with an inclined angle of 15°, without getting stuck and slipping backward.

We further examine its locomotion on an uneven, loose sand terrain with randomly distributed bumps and pits. As seen in

Downloaded from https://www.pnas.org by 98.122.129.244 on March 31, 2023 from IP address 98.122.129.244.

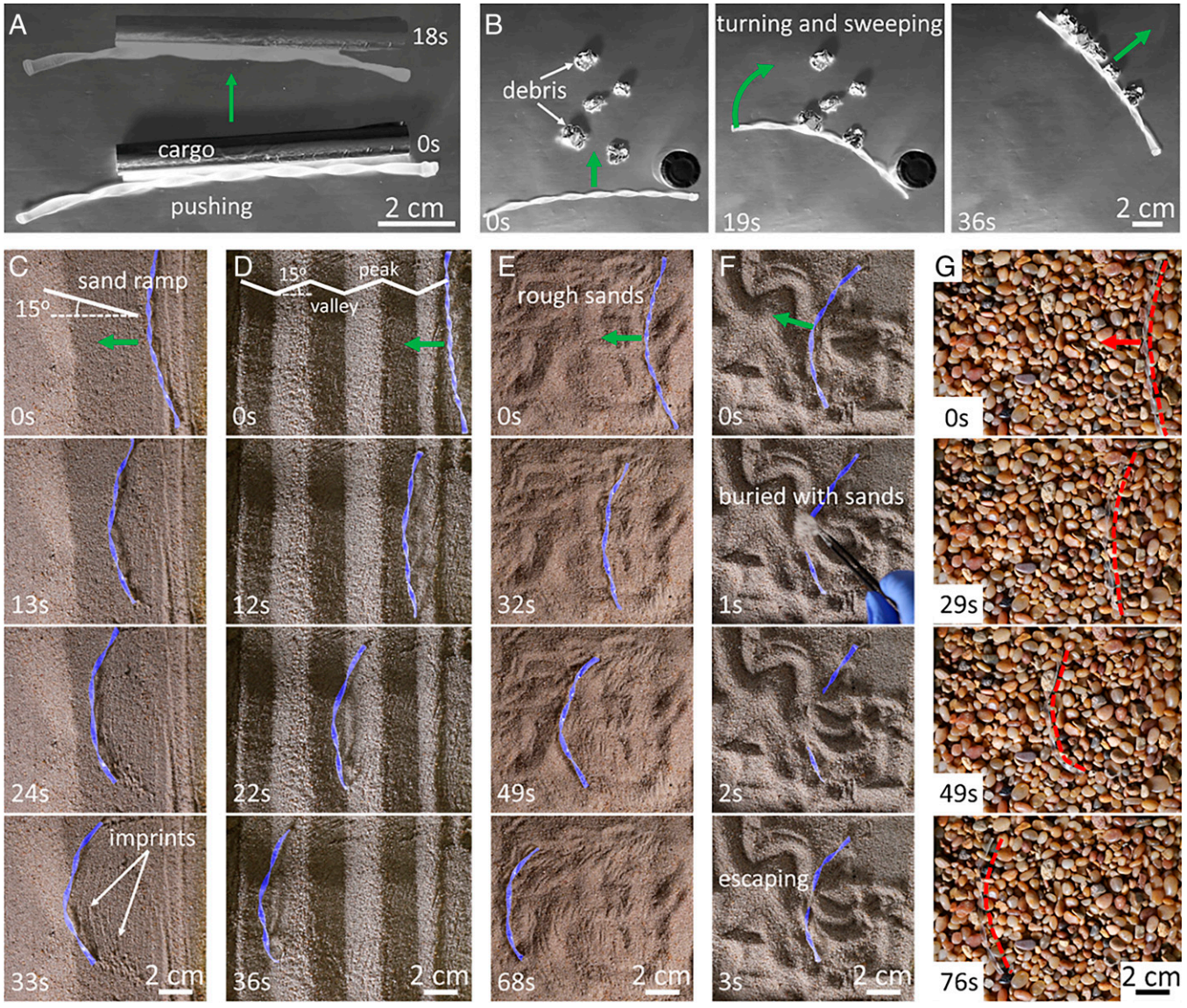

Fig. 3. Proof-of-concept cargo transport and debris cleaning, as well as self-rolling in various dry, hot loose sand and rock terrains. (*A* and *B*) Demonstration of cargo transport by pushing an alumina tube (*A*) and debris cleaning of randomly distributed alumina particles via sweeping (B). The self-rolling soft robot turns around the glass vial (Bottom Right) to sweep and collect the debris and push forward after removing the glass vial. (*C*) Self-climbing a loose sandy slope with a slope angle of 15° without slip. It burrows into the loose sand through its sharp drill bits-like twisting boundaries for enhanced traction and leaves curved imprints along the track (Bottom). (*D*) Self-rolling and cross a periodically rippled sand terrain with the same slope angle of 15° for both valleys and peaks without being stuck and slip. (*E*) Self-rolling on rough loose sand with randomly distributed bumps and pits. Broken curved imprints are observed. (*F*) Escaping from buried sand by manually burying part of its soft body with sand during its self-rolling on random rippled sand with a much higher amplitude. The twisted ribbons in (*C*–*F*) are colored in blue for better visualization. (*G*) Self-rolling on small rocks. The transparent twisted ribbons are camouflaged in the background of the rocks and red dashed curves are for better visualization. In (*C*–*G*), all the surface temperatures are the same with ~150 °C.

Fig. 3*E* and Movie S5, even though the altitudes are higher than the cross-sectional diameter of the ribbon, the twisted ribbon-based soft robot can still self-roll but leaving less and broken imprints along its curved soft body. It indicates that even though certain parts of its soft body lose their contacts with the bumpy sand, it can still utilize other dynamically changing discrete thermal contacts to drive the rolling motion. On an uneven sand terrain with much higher altitudes, we manually add sand to bury part of its soft body, it can still emerge by shedding off the sand through the twisting-induced rolling motion and continue to move forward (Fig. 3*F*). Since discrete contact is important, we create the granular foundation from tiny rocks with sizes slightly larger than the cross-sectional diameter of the twisted ribbon to examine the effect of substrate grain size versus the pitch of the contact points. Fig. 3*G* shows that the robot can successfully cross the rocks. It can also continuously roll even on a burning hot grill mesh with a more discrete surface feature (an average temperature of 200 °C, *SI Appendix*, Fig. S9*A*, Movie S3), clearly demonstrating the advantages of the twisted soft body in locomotion. When heated above T_{NI}, the ribbon also becomes transparent, offering camouflage in the background of rocks, sand, and grills (Fig. 3*G*).

SI Appendix, Fig. S9*B* summarizes its average speeds in different terrains at approximately the same surface temperature of 150 °C. As expected, the rolling speed is moderately influenced by the terrains: it is slower in the terrains with relatively larger roughness and slopes such as bumpy sand, rocks, and sand ramps. Interestingly, the average speed in granular loose terrains (i.e., flat sand and aquaria aragonites) is approximately the same as that on a hard, flat hot plate. We believe that this is due to the similar discrete thermal contacts in both terrains,

Downloaded from https://www.pnas.org by 98.122.129.244 on March 31, 2023 from IP address 98.122.129.244.

and more conformable contacts of the twisted ribbon with the discrete, loose sand.

Autonomous Obstacle Negotiation via Self-Snapping. To better understand how the soft robot interacts with unstructured environments without involving humans and external controls, we place an obstacle, here a glass vial (diameter of 2 cm), along its motion path (Fig. 4*A*). The glass vial is aligned close to the axis of symmetry of its curved soft body. After meeting the obstacle and subsequently a few trials of back and forth contacts along its axial length, seemingly like negotiation with the obstacle, the ribbon untwists itself locally and suddenly snaps through to form a flipped deep arc shape, and move away from the obstacle with its arc shape recovered (Movie S6), as opposed to continuously spinning on site as seen in the self-rolling LCE rods (30).

A closer look shows that after the ribbon contacts the hard obstacle at its vertex, the soft body transits from the shallow arc shape to an M-like shape due to the blocked motion (Fig. 4*A, ii*). As the contact point starts to slide spontaneously, the ribbon becomes slightly untwisted to increase the elastic strain energy upon deformation, resulting in a switched S-like shape (Fig. 4*A, iii*), which then quickly snaps into a deep C-like arc shape within 128 milliseconds duration to release the accumulated energy (Fig. 4*A, iv*). Slow-motion side view shows that the soft robot also slightly jumps off the hot surface during the snapping (*SI Appendix*, Fig. S10) to reduce contact and release the accumulated elastic strain energy. Then, the untwisted ribbon gradually recovers to its original shallow C-like shape as it continues to self-roll. Similar snapping is observed in those samples with more twists but taking slightly longer snapping time (*SI Appendix*, Fig. S11). We find that for the ribbons with a relatively higher twist density (> 0.37 turns/cm), the snap-through induced flipped rolling motion occurs when the initial contact point approximately falls within the middle one-third domain of the twisted ribbon, beyond which a self-turning around the obstacle at either end clockwise or counterclockwise is preferred (Fig. 4*B*).

Similar snapping occurs for both hard and soft obstacles, whether single and multiple point contacts. The snapping behavior appears independent of the radius of the obstacles, as we replace the glass vial with a small rod with an extreme small curvature (diameter of 3.1 mm) and a straight and wide ruler with an infinite curvature (*SI Appendix*, Fig. S12). Similar intermediate S-like shapes are observed immediately followed by snapping (*SI Appendix*, Fig. S12). When an array of obstacles, e.g., side-by-side glass vials, is placed (Fig. 4*C* and *SI Appendix*, Fig. S13), the single-point contact transits to multiple-point contact, similar snapping behavior is observed except that the snapping time reduces slightly to around 100 milliseconds (*SI Appendix*, Fig. S13) and the intermediate S-like shape disappears. After adding another parallel array of obstacles, the twisted ribbon continuously bounces back and forth in between (Fig. 4*C*, Movie S6). We then leave two ribbons on the hot plate by themselves. When two ribbons of opposite rolling directions meet halfway, they start to interact with each other by sliding and consequently deform into straight ribbons through multiple contacts, as a way to store the energy (Fig. 4*D*). Then, both ribbons snap almost simultaneously (within 1 s) into similar parabolic shapes with the same orientation and self-roll along the same direction. The coordinated motion has been reported in photo-initiated snapping of liquid crystal network (LCN) thin strips (48, 49), where both ends of the LCN strips are clamped to store the energy and undergo snapping upon photomechanical actuation. Here, the two ends of our twisted LCE ribbons are free to rotate: the energy storage through contact and energy release through snapping are solely induced via the soft body-environment interactions during its motion.

Understanding the Snapping Mechanism Via Simplified Modeling and Simulation. To better understand the snapping mechanism and energetics, we developed a simplified theoretical model and quasi-static FEA to analyze how the twisted LCE ribbon interacts with a single obstacle. To quantify the deformation-induced elastic strain energy change during the snapping process, we calculate its normalized elastic strain energy as a sum of the bending energy and twisting energy (50) stored in the twisted ribbon. The calculated elastic strain energy ratio in four representative states (State 0 to State 3) before and after snapping (see Fig. 4*A* and *SI Appendix*, Fig. S14) is estimated to be 1:19:5:1 (see details in *SI Appendix*), where the unstable State 1 in an S-like shape has the highest elastic strain energy. It immediately and drastically decreases by close to fourfolds via snapping through to State 2 in a deep parabolic C-like shape (Fig. 4*A*) to release the accumulated strain energy. It is followed by further release of the elastic strain energy to arrive at the dynamically stable State 3 as shown in *SI Appendix*, Fig. S14. When the twisting energy is absent in the model, i.e., the ribbon is nontwisted initially, no snap-through would occur since the elastic strain energy in the S-like shape is even lower than that of the deep C-like shape. Simplified quasi-static FEA simulation of the snapping is approximated to rigid cylindrical indentation on an arc-shaped twisted ribbon placed on a substrate, which has constrained translation but free rotation at two ends and considers temperature-induced untwisting and shrinkage upon contact (see details in *Materials and Methods*). Fig. 4*E* captures the intermediate unstable state of S-like shapes with a centered or off-centered contact (*SI Appendix*, Fig. S15), followed by sudden snapping to the inverted bent shape with the loss of contacts (Movie S7).

Intelligent Autonomous Escaping from Confined Spaces via Active, Adaptive Interactions. Last, utilizing the embodied physical intelligence, we demonstrate decision-making capability of the soft robot by autonomously escaping from confined spaces with increased complexity through active body-obstacle adaptation without any external control and human interventions.

First, two arrays of aligned obstacles (e.g., glass vials) are set to form two angled walls with a wide opening end (90° in *SI Appendix*, Fig. S16) and a narrow, confined space (30° in Fig. 5*A*), respectively. As expected, it is relatively easier and faster to escape from the 90°-angled walls after two trials of snapping-through and bounces from the walls (*SI Appendix*, Fig. S16) versus six trials from the 30°-angled walls (Fig. 5*A*, Movie S8).

Second, a simple maze-like obstacle course is tested with an enclosed wall and a diamond-shaped island in the center (see illustration in Fig. 5*B, i* and Movie S9). The enclosed wall has an exit at its top left corner. The soft robot is placed on the top right corner, away from the exit with its rolling direction facing the right wall. After two subsequent snapping against the right and top wall (Fig. 5*B, ii* and *iii*), it reverses its moving direction and meets the central diamond island. Then, it self-rotates around the top vertex of the diamond to align its soft body facing the top left side of the island. Eventually, it snaps to escape (Fig. 5*B, iv*). Its autonomous escaping capability is further verified by randomly placing the twisted ribbon at different starting locations away from the exit; its motion trajectory paths are tracked from the top view based on the center of

Downloaded from https://www.pnas.org by 98.122.129.244 on March 31, 2023 from IP address 98.122.129.244.

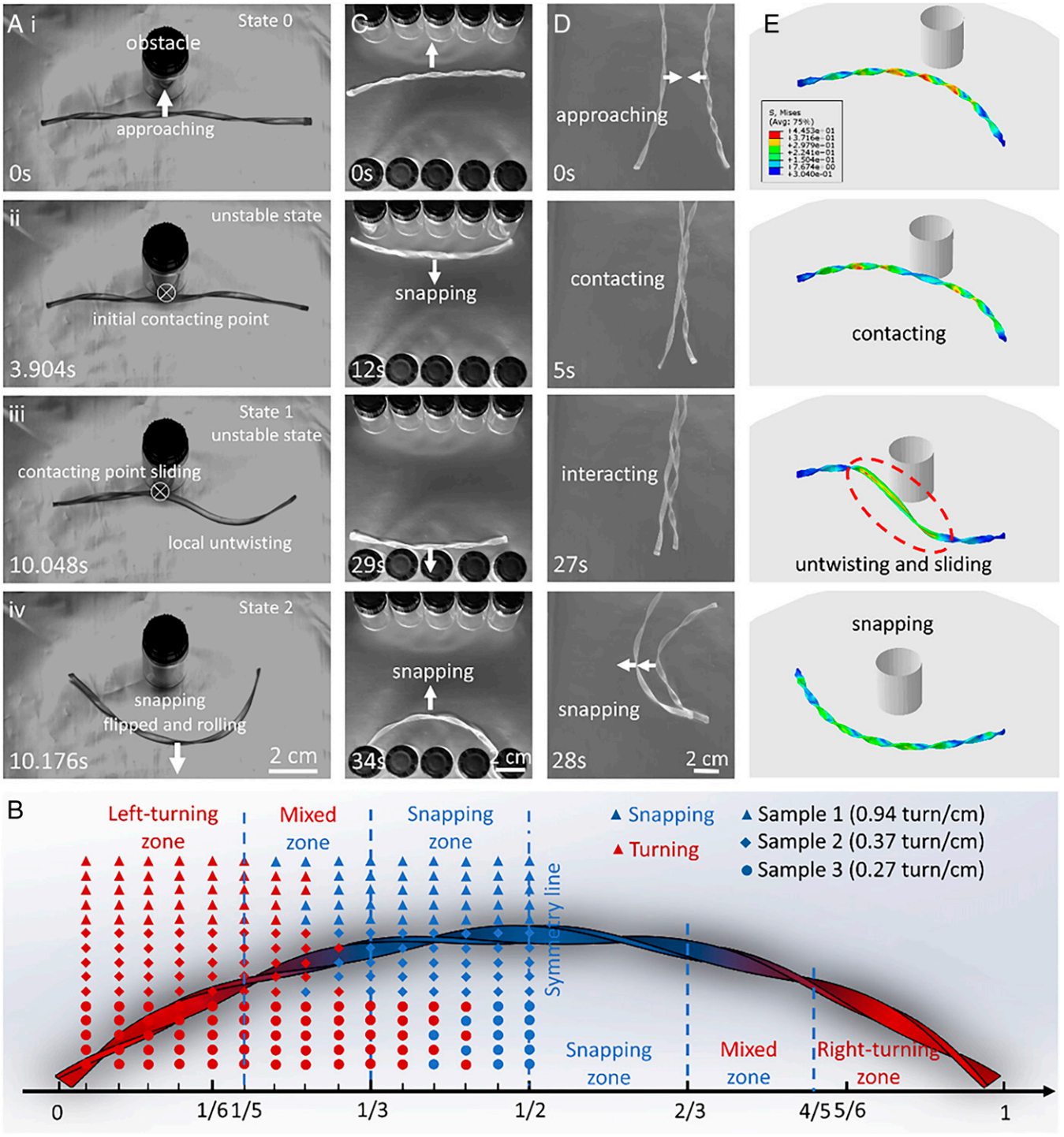

Fig. 4. Active interactions of the twisted LCE ribbons with environmental obstacles via spontaneous snapping. (*A*) Autonomously reverting of its self-rolling direction through spontaneous snapping via the active, adaptive soft body-obstacle interaction. The self-rolling curved twisted ribbon is blocked by the obstacle of a glass vial (*i*), leading to shape changes from an M-like shape (*ii*) to an S-like shape accompanied by the sliding of the contact point and local untwisting (*iii*). The unstable S-like shape quickly snaps through to an intermediate deep parabolic shape with inverted curve orientation within 128 ms. As it rolls way from the obstacle, the twisted shape is recovered. (*B*) Experimental data on the self-turning zone (highlighted in red, 0–1/5 for left turn, 4/5–1 for right turn), mixed zone (highlighted in blended blue and red, 1/5–1/3 and 2/3–4/5), and dominated snapping-through zone (highlighted in blue, 1/3–2/3) along the normalized horizontal length of the three ribbons of different twist densities at different initial contact locations with an obstacle. (*C*) Bouncing back and forth of the self-rolling ribbon between two parallel walls composed of side-by-side glass vials via multiple soft body-obstacle contact points and interactions-induced snapping. (*D*) Redirection of the two self-rolling ribbons with originally opposite moving directions. The two ribbons transit to straight shapes upon soft contact and interactions, followed by simultaneous snapping to move along the same direction. The surface temperature is ~150 °C. (*E*) FEA simulation of the snapping process in (*A*) by an approximate model of indenting of a rigid cylinder (obstacle) on a precurved twisted LCE ribbon, capturing the local untwisting, intermediate shape changes, and snapping induced loss of contact.

mass. As expected, their motion paths are distinct from each other. Depending on its starting configurations, the escaping time ranges from ~7 min to 35 min (Fig. 6 and *SI Appendix*, Fig. S17). We further test and show the successful autonomous escaping from another slightly more complex maze-like obstacle course, e.g., by replacing the island with a vertical wall to add

Downloaded from https://www.pnas.org by 98.122.129.244 on March 31, 2023 from IP address 98.122.129.244.

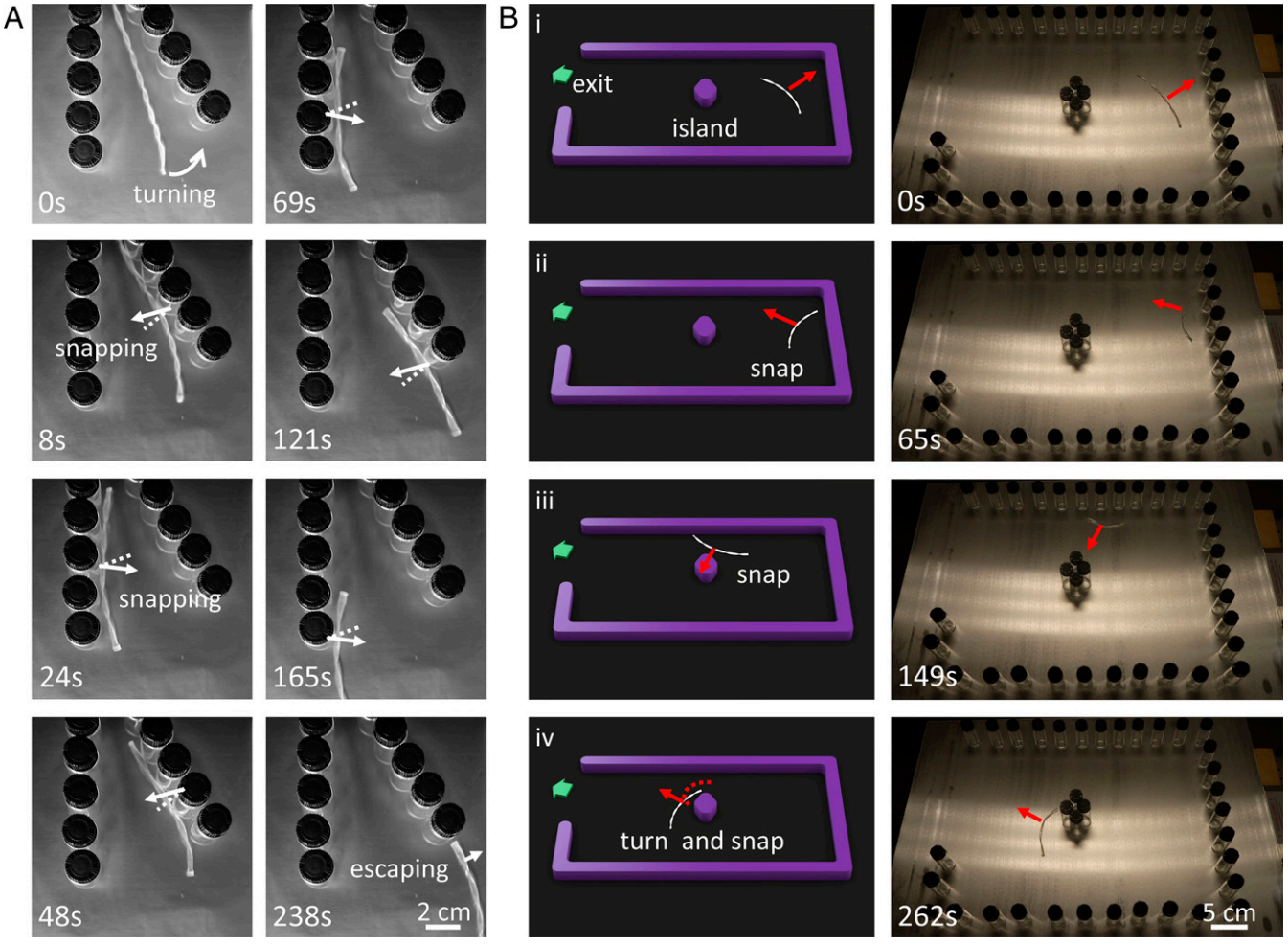

Fig. 5. Intelligent and autonomous escaping from confined spaces and a maze-like obstacle course via active and adaptive snapping and self-turning of LCE ribbons. (*A*) Autonomous escaping from a narrow and confined space between two small, angled walls (30° with two arrays of side-by-side glass vials) via multiple trials of snapping. The ribbon escaped from the open end after six trials of snapping from interacting with both walls. (*B*) One example of autonomous exiting from a simple maze-like obstacle course. Left and right column show the schematics and experimental time-lapse images of the obstacle course and the representative navigation process and interactions with the environment, respectively. The obstacle course is composed of an enclosed rectangular-shaped wall with a diamond-shaped island in the center as the obstacle and an exit in the top left corner. The wall and obstacle are modeled by glass vials in experiments (*Right*). The soft robot was placed away from the exit and autonomously exited after several snapping and turns through interaction with both the wall and the island. All the surface temperature is about 150 °C. Successful escaping is also observed at initial randomly placed positions away from the exit.

one more channel, as shown in *SI Appendix*, Fig. S18, Fig. S19, and Movie S9. The soft robots can repeatedly preform the task over several hundred cycles without degradation.

Discussion

We design and fabricate twisted LCE ribbons that harvest thermal energy via dynamic discrete contacts with a hot substrate, demonstrating autonomous locomotion in various unstructured granular terrains. Most remarkably, via spontaneous snapping, the ribbon can intelligently and autonomously negotiate and avoid obstacles by harnessing active and adaptive soft body-environment interactions without external controls, allowing for successful escaping from unstructured confined maze-like spaces. The extraordinary adaptivity are attributed to both the twisting geometry and deformation-induced elastic strain energy storage and release through reversible snapping of the twisted LCE ribbon. The strategy of embodied physical intelligence presented here enables adaptive soft body-environment interactions, thus could reduce the efforts of human intervention or use of external controls for autonomous navigation and decision making in soft robots. It will be very attractive for autonomous locomotion in extreme environments such as on hot surface roads and desserts (51) by harvesting thermal energies or combination of different stimuli for actuation.

Despite the successful demonstration of self-rolling on various granular terrains and autonomous escaping from simple maze-like obstacle courses, we note that there are several limitations of this work. First, a general multiphysics modeling and simulation is needed to better and accurately capture the observed snap-through phenomenon during its contact with an obstacle and arrays of obstacles. The future model will consider the complex thermomechanical coupling in the LCE twisted ribbon, both discrete thermal contacts and frictional contact between the twisted ribbon and the hot plate, the heat-induced concurrent shrinking and untwisting behavior in the LCE ribbon, and the interaction between the obstacle and the ribbon. Second, the temperature required to drive the self-rolling locomotion on a hot substrate is high for practical applications, e.g., on roads under the sun. This could be addressed by reducing T_{NI} using a different set of crosslinkers or changing their concentrations (52, 53). Third, the twisted ribbon would

Downloaded from https://www.pnas.org by 98.122.129.244 on March 31, 2023 from IP address 98.122.129.244.

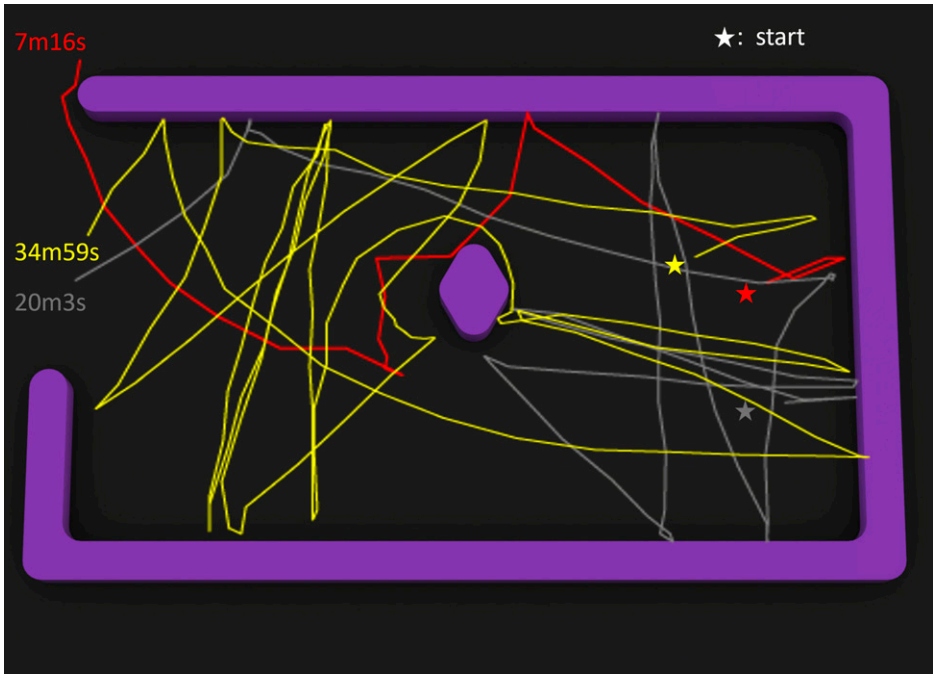

Fig. 6. Three representative escaping trajectories from the simple maze-like obstacle course. The starting points (denoted as stars, location 1 red, location 3 gray, location 5 yellow in Movie S9) are randomly selected away from the exit. Their trajectories and escaping time can be significantly different. The trajectories are captured by tracking the center of mass of the twisted ribbon.

potentially get stuck by bouncing back and forth inside the parallel channels (e.g., Fig. 4*C*). To improve its self-escaping capabilities, twisted ribbons with structural anisotropy or asymmetric geometries for a built-in slight turning motion will be explored in the future. Fourth, the terradynamics underpinning the rich phenomenon of self-rolling on challenging loose sand and rocks (Fig. 3 and Movie S5) remains to be explored (36). The complex ribbon-granular media interactions could also be influenced by the ribbon sizes and weight, and even the imposed stresses on the terrains. Future investigations are needed to address these challenges.

Materials and Methods

LCE Ribbon Fabrication. The LCE samples were synthesized by modifying previously reported thiol-acrylate Michael addition reaction method (40, 41). The liquid crystal mesogenic monomer, 1,4-bis-[4-(3-acryloyloxypropyloxy)benzoyloxy]-2-methylbenzene (RM 257), was purchased from Wilshire Technologies and utilized without further modification. In a typical synthesis process, 2 g of RM 257 was firstly fully dissolved in 0.7 g of toluene at 85 °C with magnetic stirring, followed by cooling down to room temperature. Then, 0.42 g of the chain extender 2,2′-(ethylenedioxy) diethanethiol (EDDET, Sigma Aldrich), 0.18 g of crosslinker pentaerythritol tetrakis (3-mercaptopropionate) (PETMP, Sigma Aldrich), and 0.012 g of the photoinitiator (2-hydroxyethoxy)-2-methylpropiophenone (HHMP, Sigma Aldrich) were added in the solution. The solution was then well dissolved at 85 °C and cooled down to room temperature again. Subsequently, 0.288 g of the dipropyl amine (DPA, Sigma Aldrich) solution (2 wt%, in toluene) was added in the solution that serves as the catalyst. After being fully mixed and degassed, the solution was carefully poured in the prepared mold (length 9 cm, width 3 mm, depth 1 mm). Next, the mold was placed in a closed container overnight for fully reaction. A first-cured LCE sample can be obtained after dried at 80 °C for 1 d. When the LCE ribbon was fully dried, it was uniaxially stretched to about 140% strain and twisted, followed by exposure to 365 nm ultraviolet (UV) irradiation at an intensity of 20 mJ/cm^2 for 10 min while keeping both stretching and twisting for the second stage UV curing.

Characterization Methods. The DMA (dynamic mechanical analysis) tests were performed in air using first stage partially cured with prestretching and second stage fully cured ribbon samples without twists using a dynamic mechanical analyzer (DMA 850, TA instruments). A temperature sweep was utilized from room temperature to 140 °C with ramping rate 3 °C/min. The Tan(delta) of the two samples were plotted with red lines in *SI Appendix*, Fig. S2 *A* and *B*. Notably, the first stage cured sample had a peak at ∼80 °C, corresponding to T_{NI}. However, the peak vanished after UV curing. These results are consistent with the previous study (40).

The shrinking and untwisting of the LCE ribbon at an elevated environmental temperature were performed in an oven. The temperature ramping rate is less than 3 °C/min, and the samples were conditioned for 1 extra minute to reduce overheating. The infrared videos and images were taken with an infrared camera (FLIR A655sc). The high-speed videos were taken with a high-speed camera (Fastcam SA-X2, Photron). At least three tests were performed for each condition.

The self-rolling was performed in various terrains, including flat and rigid surfaces (e.g., hot plate with metal and ceramic surfaces), loose and dry sand with different surface roughness, hot rocks, and loose aquaria aragonites. The sand, rocks, and aquaria aragonites were purchased from local vendors without further treatments. The thick sandy bed (30 to 35 mm) in Movie S5 was randomly scooped and stirred to generate loose and rough surface with randomly distributed bumps and pits. It shows that the twisted sample with a dimeter of 3 mm is able to self-roll on the loose and rough granular terrain with leaving imprints behind. For other sand terrains, the sand bed thickness (> 10 mm) is over three times higher than the sample diameter. The periodic peaks and valleys in Fig. 3*D* were carefully scraped with a 3D printed patterned object (height 6.5 mm, wavelength 50 mm) without packing the sandy surfaces.

To obtain the phase diagram of snapping and self-turning in Fig. 4*B* during the interaction between the twisted LCE ribbons and the obstacle, we placed the obstacle along their motion path at different locations. Three samples with different twist densities were examined and 5 data points were collected at each contact position, i.e., the normalized horizontal ribbon length. Each sample was examined at 15 distributed contact points of left half of the ribbon with equal distance in between due to the symmetry.

FEA Simulation. FEA simulation was performed with commercial software Abaqus/Explicit to simulate the thermal shrinking and untwisting behavior, as well as the snapping during the soft body-obstacle interactions. A twisted LCE ribbon with four twists was used as the model with length of 130 mm, width of 3 mm, and thickness of 1 mm, respectively. LCE is modeled as a linear thermoelastic material (54) with a Young's modulus of 11 MPa, Poisson's ratio of 0.3,

Downloaded from https://www.pnas.org by 98.122.129.244 on March 31, 2023 from IP address 98.122.129.244.

and anisotropic thermal expansion coefficients α_{ij} defined in a cylindrical coordinate (α_{33} along the axial length is negative to simulate the length shrinkage and $\alpha_{23} = -\alpha_{33}/2$ depending on the chirality to simulate the rotating and untwisting process around the axial length) from the experiments.

The snap-through process was simulated in a multistep quasi-static process. First, the twisted ribbon was placed on a rigid substrate and compressed to generate an arc shape that mimics the bended soft body shape during self-rolling. Second, a rigid cylinder was utilized as the obstacle to indent the twisted ribbon along the axis of symmetry of its curved soft body. This is to simulate the soft body-obstacle interaction in a quasi-static process under a displacement control. Only the two end points of the curved centerline were pinned, which allows its free bending in plane and rotation around the centerline. Third, when the obstacle contacted the twisted ribbon, the arc-shaped ribbon underwent both shrinking and untwisting. This is to approximately simulate the coupled thermomechanical effects in experiments in a simplified manner. Meanwhile, the ribbon was indented by the obstacle to deform and change shapes under the contact force. The frictionless hard contacts are assumed. When beyond a critical displacement, the ribbon spontaneously snapped to a flipped curved shape and detached from the obstacle. Snap-through with off-centered contact was also reproduced (*SI Appendix*, Fig. S15). Forth, after snapping, the ribbon returned to the initial twisted shape with temperature cooling down.

Data Availability. All study data are included in the article and/or supporting information.

ACKNOWLEDGMENTS. The authors acknowledge the help in DMA testing in B. O'Connor's laboratory, sample characterization in an oven in J. Tracy's laboratory, and infrared imaging in Y. Zhu's labortaory. J. Y. acknowledges the funding support from NSF, award # CMMI-2010717 and CMMI-2005374, and S.Y. acknowledges support from NSF, award # DMR-1410253.

1. K. C. Galloway *et al.*, Soft robotic grippers for biological sampling on deep reefs. *Soft Robot.* **3**, 23–33 (2016).
2. W. Wang, C. Li, M. Cho, S.-H. Ahn, Soft tendril-inspired grippers: Shape morphing of programmable polymer-paper bilayer composites. *ACS Appl. Mater. Interfaces* **10**, 10419–10427 (2018).
3. W. Hu, G. Alici, Bioinspired three-dimensional-printed helical soft pneumatic actuators and their characterization. *Soft Robot.* **7**, 267–282 (2020).
4. M. Wang, B.-P. Lin, H. Yang, A plant tendril mimic soft actuator with phototunable bending and chiral twisting motion modes. *Nat. Commun.* **7**, 13981–13981 (2016).
5. S. Iamsaard *et al.*, Conversion of light into macroscopic helical motion. *Nat. Chem.* **6**, 229–235 (2014).
6. C. S. Haines *et al.*, Artificial muscles from fishing line and sewing thread. *Science* **343**, 868–872 (2014).
7. C. S. Haines *et al.*, New twist on artificial muscles. *Proc. Natl. Acad. Sci. U.S.A.* **113**, 11709–11716 (2016).
8. D. R. Higueras-Ruiz, M. W. Shafer, H. P. Feigenbaum, Cavatappi artificial muscles from drawing, twisting, and coiling polymer tubes. *Sci. Robot.* **6**, eabd5383 (2021).
9. J. Xiong, J. Chen, P. S. Lee, Functional fibers and fabrics for soft robotics, wearables, and human-robot interface. *Adv. Mater.* **33**, e2002640 (2021).
10. K. E. Peyer, S. Tottori, F. Qiu, L. Zhang, B. J. Nelson, Magnetic helical micromachines. *Chemistry* **19**, 28–38 (2013).
11. W. Gao *et al.*, Bioinspired helical microswimmers based on vascular plants. *Nano Lett.* **14**, 305–310 (2014).
12. F. Qiu *et al.*, Magnetic helical microswimmers functionalized with lipoplexes for targeted gene delivery. *Adv. Funct. Mater.* **25**, 1666–1671 (2015).
13. H. Huang *et al.*, Adaptive locomotion of artificial microswimmers. *Science Adv.* **5**, eaau1532 (2019).
14. J. J. Wie, M. R. Shankar, T. J. White, Photomotility of polymers. *Nat. Commun.* **7**, 13260 (2016).
15. X. Pang, J. A. Lv, C. Zhu, L. Qin, Y. Yu, Photodeformable azobenzene-containing liquid crystal polymers and soft actuators. *Adv. Mater.* **31**, e1904224 (2019).
16. Y.-Y. Xiao, Z.-C. Jiang, Y. Zhao, Liquid crystal polymer-based soft robots. *Advanced Intelligent Systems* **2**, 2000148 (2020).
17. Z.-C. Jiang, Y.-Y. Xiao, R.-D. Cheng, J.-B. Hou, Y. Zhao, Dynamic liquid crystalline networks for twisted fiber and spring actuators capable of fast light-driven movement with enhanced environment adaptability. *Chem. Mater.* **33**, 6541–6552 (2021).
18. F. Zhai *et al.*, 4D-printed untethered self-propelling soft robot with tactile perception: Rolling, racing, and exploring. *Matter* **4**, 3313–3326 (2021).
19. T. H. Ware, M. E. McConney, J. J. Wie, V. P. Tondiglia, T. J. White, Actuating materials. Voxelated liquid crystal elastomers. *Science* **347**, 982–984 (2015).
20. Y. Xia, G. Cedillo-Servin, R. D. Kamien, S. Yang, Guided folding of nematic liquid crystal elastomer sheets into 3D via patterned 1D microchannels. *Adv. Mater.* **28**, 9637–9643 (2016).
21. H. Aharoni, Y. Xia, X. Zhang, R. D. Kamien, S. Yang, Universal inverse design of surfaces with thin nematic elastomer sheets. *Proc. Natl. Acad. Sci. U.S.A.* **115**, 7206–7211 (2018).
22. Y. Wang *et al.*, Repeatable and reprogrammable shape morphing from photoresponsive gold nanorod/liquid crystal elastomers. *Adv. Mater.* **32**, e2004270 (2020).
23. J. Liu *et al.*, Shaping and locomotion of soft robots using filament actuators made from liquid crystal elastomer–carbon nanotube composites. *Advanced Intelligent Systems* **2**, 1900163 (2020).
24. W. Hu, G. Z. Lum, M. Mastrangeli, M. Sitti, Small-scale soft-bodied robot with multimodal locomotion. *Nature* **554**, 81–85 (2018).
25. N. Bira, P. Dhagat, J. R. Davidson, A review of magnetic elastomers and their role in soft robotics. *Front. Robot. AI* **7**, 588391 (2020).
26. M. T. Tolley *et al.*, A resilient, untethered soft robot. *Soft Robot.* **1**, 213–223 (2014).
27. M. Wehner *et al.*, An integrated design and fabrication strategy for entirely soft, autonomous robots. *Nature* **536**, 451–455 (2016).
28. S. I. Rich, R. J. Wood, C. Majidi, Untethered soft robotics. *Nat. Electron.* **1**, 102–112 (2018).
29. M. Rogóż, H. Zeng, C. Xuan, D. S. Wiersma, P. Wasylczyk, Light-driven soft robot mimics caterpillar locomotion in natural scale. *Adv. Opt. Mater.* **4**, 1689–1694 (2016).
30. C. Ahn, K. Li, S. Cai, Light or thermally powered autonomous rolling of an elastomer rod. *ACS Appl. Mater. Interfaces* **10**, 25689–25696 (2018).
31. Z. Ren *et al.*, Soft-bodied adaptive multimodal locomotion strategies in fluid-filled confined spaces. *Sci. Adv.* **7**, abh2022 (2021).
32. Y. Sawa *et al.*, Shape selection of twist-nematic-elastomer ribbons. *Proc. Natl. Acad. Sci. U.S.A.* **108**, 6364–6368 (2011).
33. X. Lu, S. Guo, X. Tong, H. Xia, Y. Zhao, Tunable photocontrolled motions using stored strain energy in malleable azobenzene liquid crystalline polymer actuators. *Adv. Mater.* **29**, 1606467 (2017).
34. A. Kotikian *et al.*, Untethered soft robotic matter with passive control of shape morphing and propulsion. *Sci. Robot.* **4**, eaax7044 (2019).
35. Z.-Z. Nie *et al.*, Light-driven continuous rotating Möbius strip actuators. *Nat. Commun.* **12**, 2334 (2021).
36. C. Li, T. Zhang, D. I. Goldman, A terradynamics of legged locomotion on granular media. *Science* **339**, 1408–1412 (2013).
37. H. Marvi *et al.*, Sidewinding with minimal slip: snake and robot ascent of sandy slopes. *Science* **346**, 224–229 (2014).
38. M. Sitti, Physical intelligence as a new paradigm. *Extreme Mech. Lett.* **46**, 101340 (2021).
39. W. G. Walter, *The Living Brain* (W. W. Norton & Company, New York, Second Edition, 1963).
40. C. M. Yakacki *et al.*, Tailorable and programmable liquid-crystalline elastomers using a two-stage thiol–acrylate reaction. *RSC Advances* **5**, 18997–19001 (2015).
41. M. O. Saed, A. H. Torbati, D. P. Nair, C. M. Yakacki, Synthesis of programmable main-chain liquid-crystalline elastomers using a two-stage thiol-acrylate reaction. J. Vis. Exp. **107**, e53546 (2016).
42. M. Barnes, R. Verduzco, Direct shape programming of liquid crystal elastomers. *Soft Matter* **15**, 870–879 (2019).
43. Q. He *et al.*, Electrically controlled liquid crystal elastomer-based soft tubular actuator with multimodal actuation. *Sci. Adv.* **5**, eaax5746 (2019).
44. D. Ortiz, N. Gravish, M. Tolley, Soft robot actuation strategies for locomotion in granular substrates. IEEE Robot. Autom. Lett., **4**, 2630–2636, (2019).
45. D. Drotman, S. Jadhav, M. Karimi, P. d. Zonia, M. T. Tolley, (2017) "3D printed soft actuators for a legged robot capable of navigating unstructured terrain" in *2017 IEEE International Conference on Robotics and Automation (ICRA)*, pp 5532–5538.
46. M. Minamoto, K. Kawashima, T. Kanno, (2016) "Effect of force feedback on a bulldozer-type robot" in *2016 IEEE International Conference on Mechatronics and Automation*, pp 2203-2208.
47. G. Lee *et al.*, Series of multilinked caterpillar track-type climbing robots. *J. Field Robot.* **33**, 737–750 (2016).
48. M. R. Shankar *et al.*, Contactless, photoinitiated snap-through in azobenzene-functionalized polymers. *Proc. Natl. Acad. Sci. U.S.A.* **110**, 18792–18797 (2013).
49. A. H. Gelebart *et al.*, Making waves in a photoactive polymer film. *Nature* **546**, 632–636 (2017).
50. A. E. H. Love, *A Treatise on the Mathematical Theory of Elasticity* (Cambridge University Press, Cambridge, 4th ed, 1927).
51. Y. Zhao, H. Norouzi, M. Azarderakhsh, A. AghaKouchak, Global patterns of hottest, coldest and extreme diurnal variability on earth. *Bull. Am. Meteorol. Soc.* **102**, 1–23 (2021).
52. M. O. Saed, E. M. Terentjev, Siloxane crosslinks with dynamic bond exchange enable shape programming in liquid-crystalline elastomers. *Sci. Rep.* **10**, 6609 (2020).
53. M. O. Saed *et al.*, Molecularly-engineered, 4D-printed liquid crystal elastomer actuators. *Adv. Funct. Mater.* **29**, 1806412 (2019).
54. Z. Wang *et al.*, Three-dimensional printing of functionally graded liquid crystal elastomer. *Sci. Adv.* **6**, eabc0034 (2020).

Downloaded from https://www.pnas.org by 98.122.129.244 on March 31, 2023 from IP address 98.122.129.244.